



Original paper

Joint compensation of motion and partial volume effects by iterative deconvolution incorporating wavelet-based denoising in oncologic PET/CT imaging



Sahar Rezaei^{a,b}, Pardis Ghafarian^{c,d,*}, Abhinav K. Jha^{e,f}, Arman Rahmim^{g,h}, Saeed Sarkar^b,
 Mohammad Reza Ay^{a,b}

^a Department of Medical Physics and Biomedical Engineering, Tehran University of Medical Sciences, Tehran, Iran

^b Research Center for Molecular and Cellular Imaging (RCMCI), Tehran University of Medical Sciences, Tehran, Iran

^c Chronic Respiratory Diseases Research Center, National Research Institute of Tuberculosis and Lung Diseases (NRITLD), Shahid Beheshti University of Medical Sciences, Tehran, Iran

^d PET/CT and Cyclotron Center, Masih Daneshvari Hospital, Shahid Beheshti University of Medical Sciences, Tehran, Iran

^e Department of Biomedical Engineering, Washington University in St. Louis, USA

^f Mallinckrodt Institute of Radiology, Washington University in St. Louis, USA

^g Departments of Radiology and Physics, University of British Columbia, Vancouver, Canada

^h Department of Integrative Oncology, BC Cancer Research Center, Vancouver, Canada

ARTICLE INFO

Keywords:

¹⁸F-FDG PET/CT
 Reconstruction algorithm
 PSF
 TOF
 Combined compensation
 Respiratory motion
 Partial volume effect
 Quantification
 Lung cancer

ABSTRACT

Objectives: We aim to develop and rigorously evaluate an image-based deconvolution method to jointly compensate respiratory motion and partial volume effects (PVEs) for quantitative oncologic PET imaging, including studying the impact of various reconstruction algorithms on quantification performance.

Procedures: An image-based deconvolution method that incorporated wavelet-based denoising within the Lucy-Richardson algorithm was implemented and assessed. The method was evaluated using phantom studies with signal-to-background ratios (SBR) of 4 and 8, and clinical data of 10 patients with 42 lung lesions ≤ 30 mm in diameter. In each study, PET images were reconstructed using four different algorithms: OSEM-basic, PSF, TOF, and TOFPSF. The performance was quantified using contrast recovery (CR), coefficient of variation (COV) and contrast-to-noise-ratio (CNR) metrics. Further, in each study, variabilities arising due to the four different reconstruction algorithms were assessed.

Results: In phantom studies, incorporation of wavelet-based denoising improved COV in all cases. Processing images using proposed method yielded significantly higher CR and CNR particularly in small spheres, for all reconstruction algorithms and all SBRs ($P < 0.05$). In patient studies, processing images using the proposed method yielded significantly higher CR and CNR ($P < 0.05$). The choice of the reconstruction algorithm impacted quantification performance for changes in motion amplitude, tumor size and SBRs.

Conclusions: Our results provide strong evidence that the proposed joint-compensation method can yield improved PET quantification. The choice of the reconstruction algorithm led to changes in quantitative accuracy, emphasizing the need to carefully select the right combination of reconstruction-image-based compensation methods.

1. Introduction

FDG PET/CT imaging has had a major influence in cancer imaging for many clinical tasks including lesion detection, staging and monitoring therapy response [1–3]. Nevertheless, respiratory motion and partial volume effects (PVEs), two of the most important causes of

image degradation in lung cancer imaging, have been observed to significantly hamper PET image quality and quantification, in particular in small and low-uptake lesions [4–6]. For example, in lung lesions, a displacement of 4.9–20 mm due to respiratory motion can result in notable errors in tumor localization and quantification [7–9]. Several methods have been proposed for compensation of respiratory motion in

* Corresponding author at: Chronic Respiratory Diseases Research Center, National Research Institute of Tuberculosis and Lung Diseases (NRITLD), Shahid Beheshti University of Medical Sciences, Tehran 19569-44413, Iran.

E-mail address: pardis.ghafarian@sbmu.ac.ir (P. Ghafarian).

<https://doi.org/10.1016/j.ejmp.2019.10.031>

Received 1 April 2019; Received in revised form 29 September 2019; Accepted 17 October 2019

1120-1797/© 2019 Published by Elsevier Ltd on behalf of Associazione Italiana di Fisica Medica.

PET images, such as respiratory gating, data-driven respiratory gating, motion-free method, banana artefact management and deconvolving the reconstructed image with the motion-blurring kernel (MBK), referred to as deconvolution methods [10–12]. Similarly, PVEs, which result from the finite spatial resolution of PET scanners, limit lesion detectability and accurate quantification [13–15]. Several methods have been proposed to overcome PVEs limitations [16–18], including deconvolution-based methods. However, using deconvolution methods lead to significant noise enhancement. Previous work [19] has shown that incorporation of wavelet-based denoising inside the deconvolution operation can substantially diminish noise levels without significantly degrading intensity recovery. Another class of methods have investigated combined compensation of respiratory motion and PVEs [20–22]. These studies demonstrated that, in thoracic PET imaging, quantification of PET uptake values can be substantively improved by combined compensation. Apostolova et al [23] investigated the influence of combined compensation on quantification of small solitary pulmonary nodules (SPNs) in experimental phantom and patient data and concluded that, in combined compensation, standardized uptake value (SUV) increased up to 46% compared with PVEs-only compensation.

In recent years, iterative reconstruction algorithms have been improved by introducing new reconstruction algorithms such as point-spread-function modeling (PSF) and incorporating time-of-flight (TOF) information. PET images reconstructed with PSF modeling and/or TOF result in improved PET-based quantification and can increase the SNR and contrast for lesions [24–26]. Merlin et al [27] reported significantly improved detection performance for lung lesions after PVEs compensation using a deconvolution algorithm within the PSF reconstruction process. Recent studies also reported that PSF modelling and/or TOF-based reconstructions improved image quality as well as lesion detectability, in particular in small lesions [28–30]. Rogasch et al [31] have shown in a clinical study of 28 liver metastases that quantitative evaluation can be influenced when using either PSF or TOF protocols for radiotherapy or follow-up purposes in different tumour-to-background ratios.

However, very few studies have investigated the simultaneous compensation of respiratory motion and PVEs [20–23]. More importantly, as we know, there have been no studies on the impact of combined compensation of respiratory motion and PVEs in conjunction with iterative reconstruction algorithms on quantification. Therefore, the first objective of this study was to propose an image-based deconvolution method that incorporated wavelet-based denoising for joint compensation of respiratory motion and PVEs in image space. The second main objective of this study was to quantitatively evaluate the variability in quantification performance when the combined compensation of respiratory motion and PVEs was used with different iterative reconstruction algorithms for different SBRs.

2. Material and methods

2.1. Phantom studies

We utilized the National Electrical Manufacturers Association (NEMA) body phantom with six spheres of diameters 10, 13, 17, 22, 28, and 37 mm. Three spheres of the phantom (10, 17 and 28 mm diameter) were filled with ^{18}F -FDG solution, using a signal-to-background (SBR) of 4:1 and 8:1, whereas the other spheres (13, 22 and 37 mm) were filled with water. The background activity level of 4.78 kBq/mL was used in our phantom study. In order to simulate respiratory motion using NEMA phantom, we utilized a dynamic in-house platform that was designed to move phantom with sinusoidal motion profiles in the axial and lateral direction. First, the phantom was placed on the platform and scanned without any motion, yielding a static image. Next, in order to obtain an image with motion effect, the platform was moved along the longitudinal axis of the scanner with uniform velocity and 5

sec cycle. The peak-to-peak amplitudes were 20 and 26 mm for 4:1 and 8:1 SBRs, respectively.

2.2. Patients study

In this study, FDG-PET/CT images of 10 patients (3 females; 7 males; mean body mass index: $25.8 \pm 2.6 \text{ kg/m}^2$) with non-small cell lung cancer (NSCLC) were retrospectively evaluated. The analysis was performed with 42 lesions ≤ 30 mm in diameter. All patients fasted for at least 6 h before PET/CT imaging. The PET/CT scan was acquired 60.8 ± 1.5 min after ^{18}F -FDG injection. The administered activity of ^{18}F -FDG was 331.4 ± 71.0 MBq in conformity with the European Association of Nuclear Medicine guidelines [32].

2.3. Data acquisition and image reconstruction

Data were acquired with Discovery 690 PET/CT (GE Healthcare, Milwaukee, Wisconsin, USA). All data were reconstructed with various reconstruction algorithms: (1) OSEM-basic = ordered subset expectation maximization (OSEM) with no PSF or TOF, (2) PSF = OSEM with PSF only, (3), TOF = OSEM with TOF only and (4) TOFPSF = OSEM with TOF and PSF. The reconstruction parameters for TOF algorithms (e.g., TOF and TOFPSF) were 2 iterations and 18 subsets, and those for non-TOF algorithms (e.g., OSEM-basic and PSF) were 3 iterations and 18 subsets. 10 min scan time [27] was applied per bed position and the image matrix for emission data was 256×256 with 2.73 mm pixel size. CT imaging was performed for attenuation correction using 100 kVp, 80 mA and 1 s rotation time with 3.75 mm slice thickness.

2.4. Combined compensation for partial volume effects and respiratory motion

We now describe our development of a post-reconstruction method for combined compensation of respiratory motion and PVEs. Our method is motivated by the approach suggested by Bousson et al. [19], although that method was in the context of compensating PVEs and did not model the effect of motion. The degraded PET image, denoted by I , can be modeled as a convolution between the motion blurring kernel, denoted by MBK, the point spread function of the PET system, denoted by PSF, and the original tracer distribution, denoted by O [21], as below:

$$I = O \otimes \text{PSF} \otimes \text{MBK} + N \quad (1)$$

where N is an additive noise and the symbol \otimes refers to the convolution operation. It is clear that a deconvolution-based approach could be used to restore the degraded PET image. In the first step, for the determination of the MBK, we used the method proposed by Xu et al. [33]. In this method, the blur direction was identified by applying a derivative operation on the blurry image and finding the maximum intensity value of the first-order gradient image in all directions. The minimum of maximum intensity values determined the blur direction. After that, the blur extent was computed by applying a high-pass filter, computing auto-correlation of all filtered image lines and averaging them. The minimum value of the auto-correlation function yielded the value of blur extent. The motion blur direction and extent identified using directional derivative and correlation analysis were used to estimate the MBK.

In the next step, to compensate for PVEs, the system PSF was modeled as a spatially varying Gaussian kernel. The full-width-at-half-maximum (FWHM) of this Gaussian kernel was measured by imaging a multiple line sources scan, which was embedded in air and positioned at the various places in the PET field of view (FOV) and reconstructed with OSEM-basic and TOF reconstruction algorithms. Finally, the estimated MBK and PSF were applied into the post-reconstruction iterative deconvolution process. The deconvolution was performed using the iterative Lucy-Richardson (LR) algorithm. The LR algorithm can be

described as:

$$O^{n+1} = O^n \left[\frac{I}{\text{PSF}_{\text{Total}} \otimes O^n} \otimes \text{PSF}_{\text{Total}}^T \right]$$

$$\text{PSF}_{\text{Total}} = \text{PSF} \otimes \text{MBK} \quad (2)$$

where n is the LR deconvolution iteration number, O^n and O^{n+1} denote the estimates of the output image at the n and $(n + 1)$ iteration, and $\text{dPSF}_{\text{Total}}^T$ denotes the transpose of the $\text{PSF}_{\text{Total}}$.

The main challenge encountered by the iterative deconvolution process is noise amplification. A common approach for noise compensation is performing denoising during deconvolution. In this study, we implemented a wavelet-based denoising scheme [19] as follows. A residual for the n th iteration, denoted by R^n and defined as $R^n = I - \text{PSF}_{\text{Total}} \otimes O^n$, was first obtained for each iteration of the LR deconvolution. Taking the notation regarding the residual into account, Eq. (2) can be rewritten as:

$$O^{n+1} = O^n \left[\frac{\text{PSF}_{\text{Total}} \otimes O^n + R^n}{\text{PSF}_{\text{Total}} \otimes O^n} \otimes \text{PSF}_{\text{Total}}^T \right] \quad (3)$$

Next, 3D isotropic undecimated wavelet transform (IUWT) was applied on the residual with a bicubic-spline filter, yielding a set of wavelet coefficients that described the residual. In our work, the residual was decomposed for up to 3 levels. In the next step, wavelet thresholding using the BlockShrink method [34] was applied to denoise the data. In this method, the threshold value is estimated locally based on the value of the neighbor wavelet coefficients. For this purpose, first, the wavelet coefficients of each subband were divided into $L \times L$ blocks, and then the optimal block size and threshold values were obtained by minimizing Stein's unbiased risk estimate (SURE). After the denoising process, the inverse wavelet transform was applied to restore the image [35].

Note that the proposed post-reconstruction method was only applied to images reconstructed with non-PSF algorithms (OSEM-basic and TOF). For the images reconstructed using PSF algorithms (PSF and TOFPSF), only the motion compensation aspect of the deconvolution operation with denoising step was performed.

2.5. Assessment strategy

Image quality obtained using the various reconstruction algorithms before and after compensation was quantified using the contrast recovery (CR), coefficient of variation (COV) and CNR. The contrast recovery for hot spheres was calculated as follows:

$$\text{CR} = \frac{C_j/C_{\text{bkg}} - 1}{\text{SB}_{\text{ratio}} - 1} \times 100\%, \quad (4)$$

where C_j and C_{bkg} , are the mean value of the sphere and the background volumes of interest (VOIs), respectively, and SB_{ratio} represents the actual SBR. For cold spheres, the contrast recovery was given by

$$\text{CR}_{\text{cold}} = (1 - C_j/C_{\text{bkg}}) \times 100\%, \quad (5)$$

The COV was calculated as below:

$$\text{COV} = \frac{\sigma_{\text{bkg}}}{C_{\text{bkg}}} \times 100\%, \quad (6)$$

where σ_{bkg} is the mean standard deviation (SD) of the intensity values in the background VOI. We also calculated CNR as the ratio of the mean value of a VOI that surrounded the tumor minus the mean value in the background VOIs over the mean SD in the background VOIs, i.e.

$$\text{CNR} = \frac{C_j - C_{\text{bkg}}}{\sigma_{\text{bkg}}}, \quad (7)$$

Note that VOIs were drawn based on the CT images.

In this study, we calculated the relative difference of all the metrics for various reconstruction algorithms between both sets of images

(compensated vs uncompensated). Box and Whisker analysis was also applied for comparison among the different reconstruction algorithms. Additionally, inter-method differences were obtained for PSF and TOF by comparing the corresponding PSF vs non-PSF algorithms (PSF vs OSEM-basic; TOFPSF vs TOF) and corresponding TOF vs non-TOF algorithms (TOF vs OSEM-basic; TOFPSF vs PSF), respectively. Statistical analysis was performed using SPSS, version 19.0 (IBM Corp., Armonk, New York, USA). Differences between images before and after compensation using the proposed method were evaluated by paired t test and Wilcoxon's signed-rank test for the normal and non-normal distribution, respectively.

3. Results

3.1. Phantom data

The images processed with the proposed compensation method (hereafter referred to as compensated images) were first compared with the static images as well as images that were not processed using proposed method (hereafter referred to as uncompensated images). We emphasize again that the combined compensation was only applied to images reconstructed with non-PSF algorithms (OSEM-basic and TOF). For the images reconstructed using PSF algorithms (PSF and TOFPSF), only motion compensation was performed.

To evaluate the impact of the denoising method and obtain the optimum deconvolution iteration number, the LR deconvolution was performed with and without BlockShrink denoising in the different number of iterations. The results for the various iteration numbers of the LR deconvolution are shown in Fig. 1. The higher iteration number of deconvolution yields a higher COV but allows better contrast recovery. However, the use of wavelet-based denoising with post-deconvolution led to a significant decline of the COV values compared to without denoising in all reconstruction algorithms (paired t test; each $P < 0.05$). For both SBRs and all spheres, applying five iterations in LR deconvolution yielded a good balance between COV and contrast recovery. Therefore, we used five deconvolution iterations of the proposed method. Due to the same conclusions, the plots for 4:1 SBR is not shown.

Note that the blur extent were estimated as 19.2 and 25.1 mm, and the corresponding blur directions were -89° and 90° for 4:1 and 8:1 SBRs, respectively. The true values of blur extent and blur direction were 20 mm and $\pm 90^\circ$ for 4:1 SBR, respectively, and 26 mm and $\pm 90^\circ$ for 8:1 SBR.

Contrast recovery for static, uncompensated and compensated images in hot spheres for SBR 8:1 is illustrated in Fig. 2. For all reconstruction algorithms, there was a significant increase in contrast recovery for motion-only and combined compensated images compared to the uncompensated images (paired t test; each $P < 0.05$). Further, contrast recovery improvement was seen for the smallest hot sphere with more intensity. The relative contrast recovery for 10 mm sphere diameter was increased by 61.5%, 78.6%, 66.6% and 71.9% for OSEM-basic, PSF, TOF and TOFPSF with only motion compensation, respectively, and 90.2% and 87.1% for combined compensation of OSEM-basic and TOF.

Fig. 3 presents the results of the contrast recovery in cold spheres for static, uncompensated and compensated images at SBR 8:1. In the compensated images, all reconstruction algorithms provided a higher contrast recovery compared to uncompensated images. Furthermore, the relative contrast recovery for the smallest cold sphere was increased by 16.0%, 26.9%, 18.0% and 25.7% for OSEM-basic, PSF, TOF and TOFPSF with only motion compensation, respectively, and 28.8% and 29.4% for combined compensation of OSEM-basic and TOF. Note that for both hot and cold spheres, the 4:1 ratio showed similar results (for conciseness, these results not presented).

Table 1 reports the percentage increase of CNR in images reconstructed using various algorithms and then compensated using the

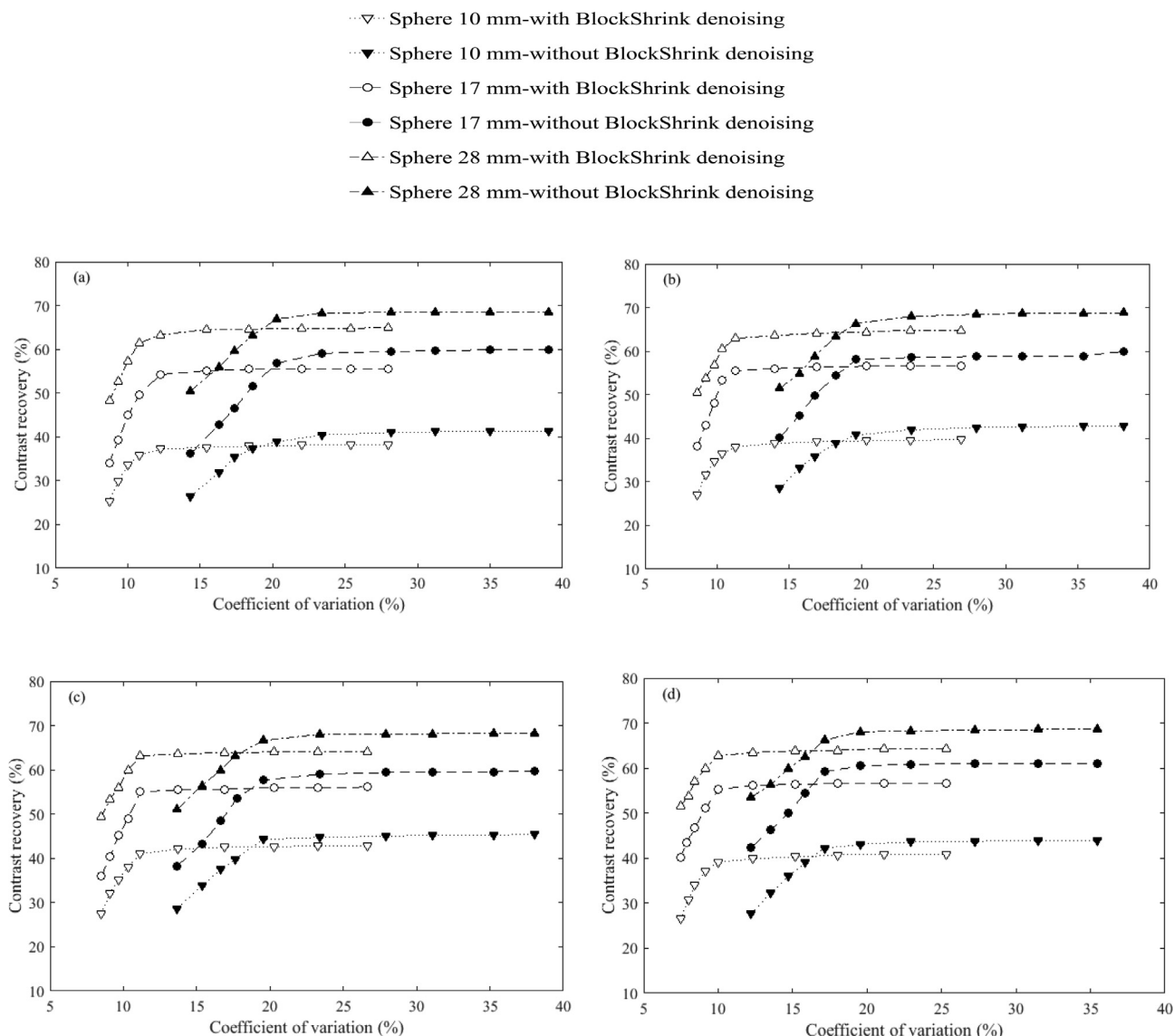


Fig. 1. Phantom data. Performance of the compensation method for (a) OSEM-basic, (b) PSF, (c) TOF, (d) TOFPSF reconstructions using the different number of post-deconvolution iterations for 3 hot spheres of the NEMA phantom in 8:1 ratio, with and without BlockShrink denoising method. Each point of the curves corresponds to an iteration number (varying from 1 to 10 reconstruction iterations).

proposed method in comparison to uncompensated images. After compensation, CNR enhancement was seen for all hot spheres with more impact for smaller spheres. Furthermore, the mean CNR in all spheres was increased by 48.4%, 41.9%, 43.9% and 40.5% for OSEM-basic, PSF, TOF and TOFPSF, respectively, in comparison with the uncompensated images for 4:1 SBR and 66.2%, 54.0%, 61.7% and 48.9% for 8:1 SBR. Thus, for all the reconstruction algorithms and for both SBRs, the mean CNR significantly improved after compensation was performed (paired *t* test; each *P* < 0.05).

Table 2 shows the inter-method CNR differences (%) for PSF vs non-PSF and TOF and non-TOF algorithms. It can be seen that, for 4:1 SBR and smaller hot sphere, TOF yielded higher CNR compared to TOFPSF. However, for larger hot spheres, TOFPSF yielded higher CNR than TOF. Further, TOFPSF yielded higher CNR than TOF for all hot sphere in 8:1 SBRs. In both SBRs, PSF and TOF yielded higher CNR than OSEM-basic for all hot spheres. TOFPSF also yielded higher CNR than PSF for all hot sphere in both SBRs. Note that the mean inter-method CNR differences were higher for all hot sphere in 8:1 SBR compared to 4:1 SBRs.

3.2. Patient data

For quantitative evaluation, all clinical datasets were reconstructed with the various algorithms and then compensated only for motion or both PVEs and motion, depending on the reconstruction algorithm. Fig. 4 shows images from one male patient with a BMI of 23 kg/m². The motion amplitude was estimated as 3 pixels, and the corresponding blur direction was 71°. The relative difference of the contrast recovery in compensated images compared to the corresponding uncompensated images was 32.9% and 35.7% for PSF and TOFPSF with only motion compensation, respectively, and 36.6% and 37.5% for combined compensation of OSEM-basic and TOF. In the compensated images, all reconstruction algorithms provided a significantly higher contrast recovery compared to uncompensated images (Wilcoxon’s signed-rank test; each *P* < 0.05).

Fig. 5 shows box and whisker plots of the relative difference (%) of the CNR in compensated images for various reconstruction algorithms compared to uncompensated images in patients with 42 lesions ≤ 30 in diameter. The median value was 46.5%, 42.4%, 49.1% and 45.7% for OSEM-basic, PSF, TOF, and TOFPSF, respectively. The relative

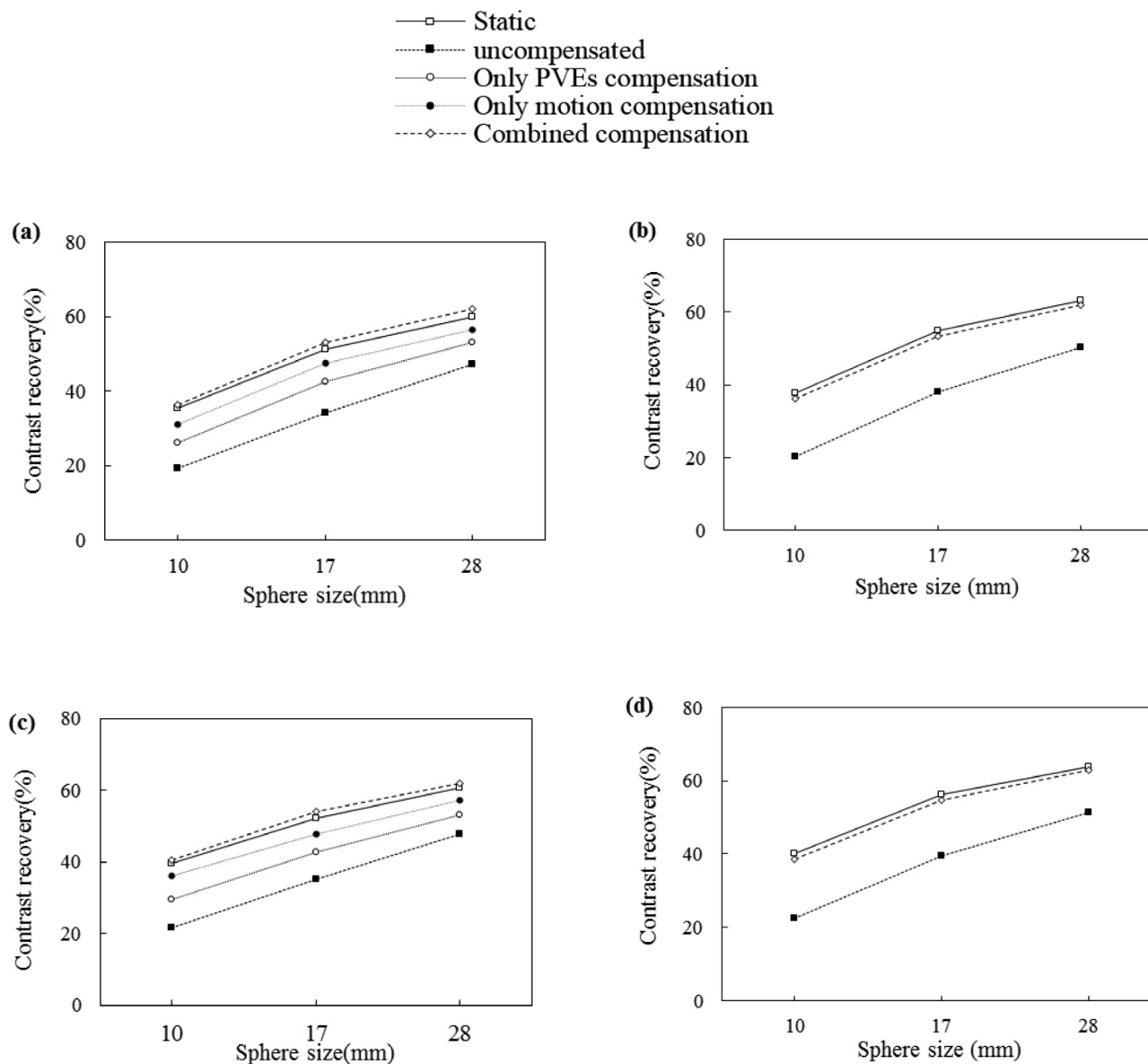


Fig. 2. Phantom data. Comparison between the contrast recovery (%) in static, uncompensated and compensated images with 8:1 SBR in hot spheres for (a) OSEM-basic, (b) PSF (c) TOF and (d) TOFPSF.

difference (%) between the minimum and maximum of median value was 13.6% when various reconstruction algorithms (OSEM-basic, PSF, TOF and TOFPSF) were applied.

4. Discussion

In clinical PET imaging, deteriorations in image quality due to respiratory motion and PVEs present major challenges. Further, given the wide variety of iterative reconstruction algorithms, it is unclear what the best combination of reconstruction and post-processing algorithm is. To address these challenges, we assessed the application of post-reconstruction LR deconvolution with BlockShrink denoising to compensate for both PVEs and motion, in conjunction with four different iterative reconstruction algorithms. Performance of the proposed compensation method was assessed with NEMA phantom studies and patient data.

Our phantom study demonstrated that incorporation of wavelet-based denoising inside the LR deconvolution can significantly control noise amplification due to the deconvolution process (Fig. 1). Another observation is that motion-only or combined compensation improved

contrast recovery values for all reconstruction algorithms (Figs. 2 and 3). Some previous studies [19,27,33] have shown that using deconvolution methods with denoising for either PVE compensation or motion compensation can lead to higher CR with acceptable noise levels. Our results show that using deconvolution method with denoising provides improved COV and contrast recovery even for joint compensation tasks.

Moreover, our results show that, in uncompensated images, contrast recovery decreased by decreasing sphere size, as would be expected due to the motion. A decrease in the sphere size from 28 to 10 mm in diameter led to the CR decreasing by 70.5%, 70.6%, 68.2% and 70.7% for OSEM-basic, PSF, TOF and TOFPSF, respectively, for 4:1 SBR and 59.2%, 59.7%, 54.7% and 56.3% for 8:1 SBR. In this regards, Siman et al [36] mentioned that motion could decrease activity concentration by 20–80% depending on tumor size and motion amplitude.

We also observed that higher CNR values were obtained for all sphere and both SBRs in compensated images (Table 1). Previous studies have shown that using TOF algorithms can lead to improved contrast-noise trade-off performance relative to non-TOF algorithms, especially for small lesion [37,38]. Our results demonstrated that for smaller sphere in compensated images, TOF and TOFPSF provided

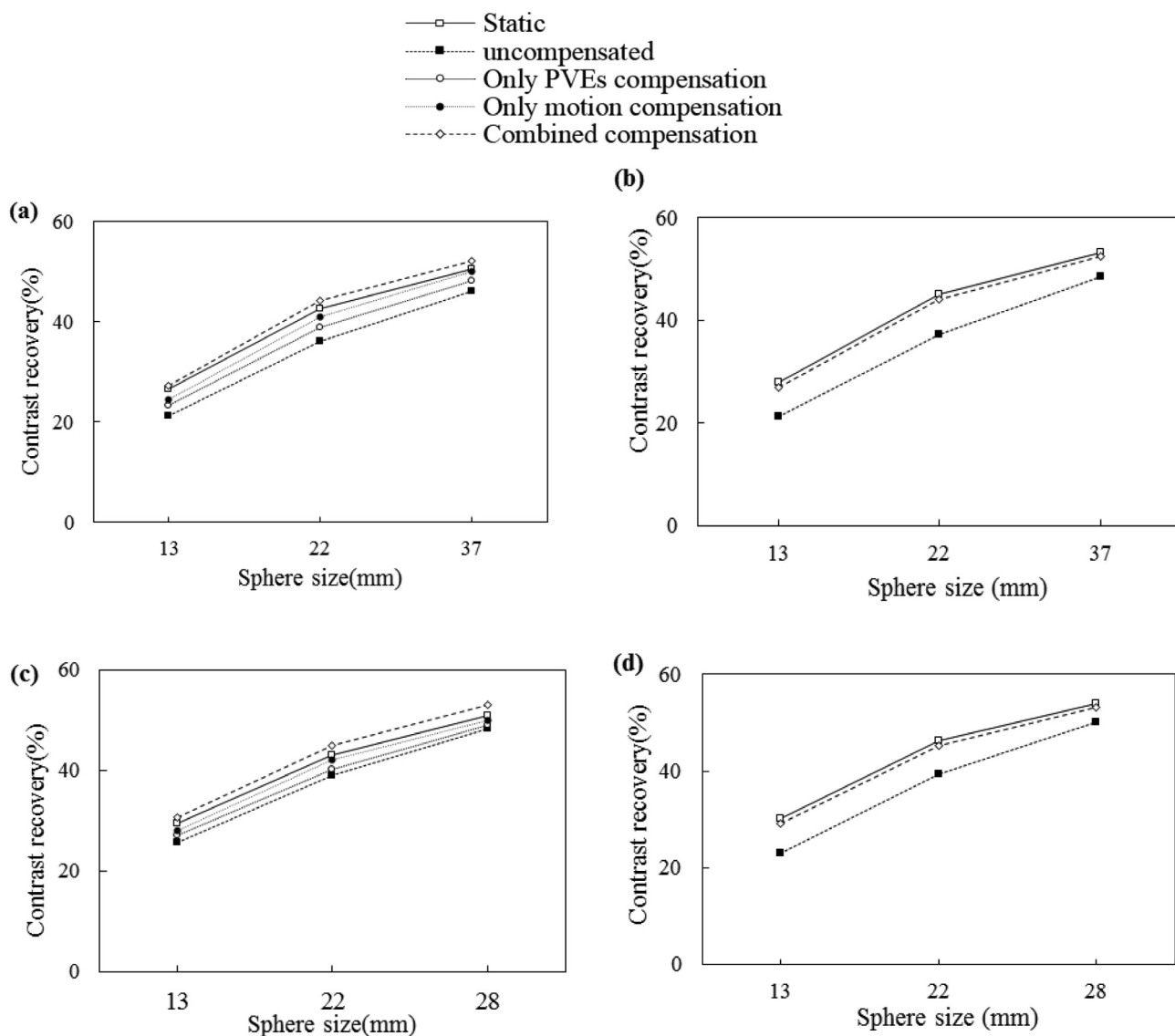


Fig. 3. Phantom data. Comparison between the contrast recovery (%) in static, uncompensated and compensated images with 8:1 SBR in cold spheres for (a) OSEM-basic, (b) PSF (c) TOF and (d) TOFPSF.

Table 1

Phantom data. Increase (%) of the CNR for compensated images relative to the uncompensated image in PSF algorithms with only motion compensation and non-PSF algorithms with combined compensation for both 4: 1 and 8:1 SBRs.

	OSEM-basic	PSF	TOF	TOFPSF
4:1 ratio				
Sphere 10 mm	85.8	84.7	80.0	82.0
Sphere 17 mm	43.3	32.1	37.5	31.1
Sphere 28 mm	16.1	9.02	14.2	8.42
8:1 ratio				
Sphere 10 mm	98.1	93.1	96.9	82.9
Sphere 17 mm	69.7	49.9	62.1	45.9
Sphere 28 mm	30.9	19.0	26.0	17.9

higher CNR versus the corresponding non-TOF algorithms (Table 2). The relative differences were lower for TOFPSF (TOFPSF vs PSF) relative to TOF (TOF vs OSEM-basic). Overall, the TOFPSF algorithm empirically yielded the highest improvements for all sphere sizes. Thus, we infer that it is more helpful to perform PSF modeling while reconstruction instead of post-processing.

Retrospective quantitative analysis of clinical FDG PET/CT studies

Table 2

Phantom data. Relative CNR differences (%) for compensated images. Comparison of PSF vs non-PSF (left) as well as TOF vs non-TOF algorithms (right).

	PSF vs OSEM-basic	TOFPSF vs TOF	TOF vs OSEM-basic	TOFPSF vs PSF
4:1 ratio				
Sphere 10 mm	5.49	-5.68	16.4	6.56
Sphere 17 mm	14.0	11.6	10.2	7.71
Sphere 28 mm	13.4	12.0	9.83	8.39
8:1 ratio				
Sphere 10 mm	9.27	4.31	17.1	12.5
Sphere 17 mm	9.30	9.05	9.50	9.25
Sphere 28 mm	7.53	8.27	8.39	9.12

on lymph node metastases by Akamatsu et al. [39] revealed notable improvements when including PSF and TOF. On the basis of our clinical findings, contrast recovery and CNR for compensated images with TOF and TOFPSF were superior to another algorithm in non-PSF and PSF algorithms, respectively. Although only the blurring effect of the

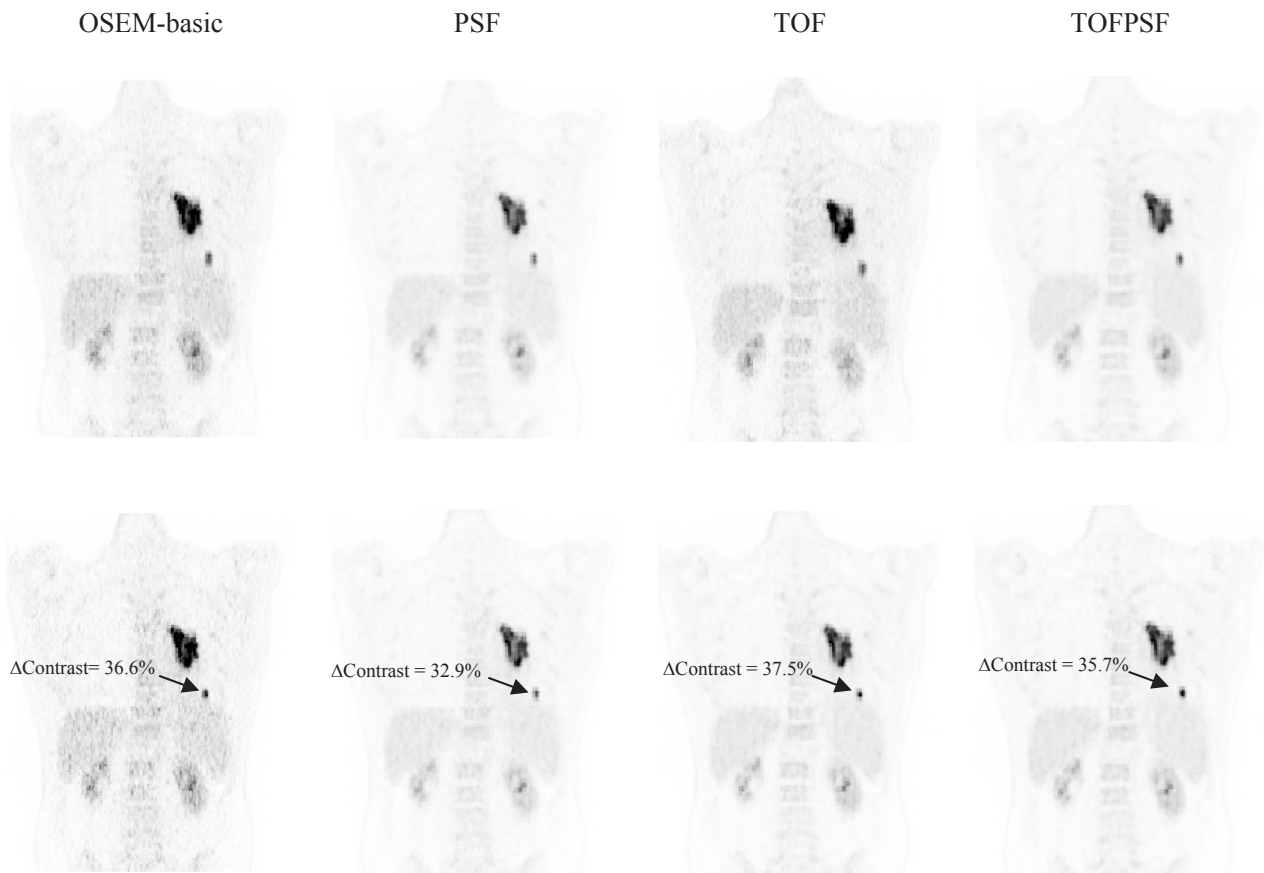


Fig. 4. Patient data. Coronal PET images of a 42-year-old man with NSCLC; First row: before proposed compensation method, second row: after proposed compensation method.

patient motion can be compensated with our proposed method, actually our results showed that TOF algorithms can lead to lowering of another specific artefact, namely the banana-shaped artefact, which is one of the most common artefacts induced by the patient motion due to the changing photon attenuation inside the patient [40,41]. This is consistent with other studies showing the TOF localizes the error

propagation and reduces certain image artefacts [42]. Moreover, in conformity with previous studies [43–46], we found that in compensated images, switching from non-TOF to TOF modelling led to improved quantitative accuracy.

The present work highlights the effect of the choice of the PET reconstruction algorithm on quantitative accuracy in the compensated

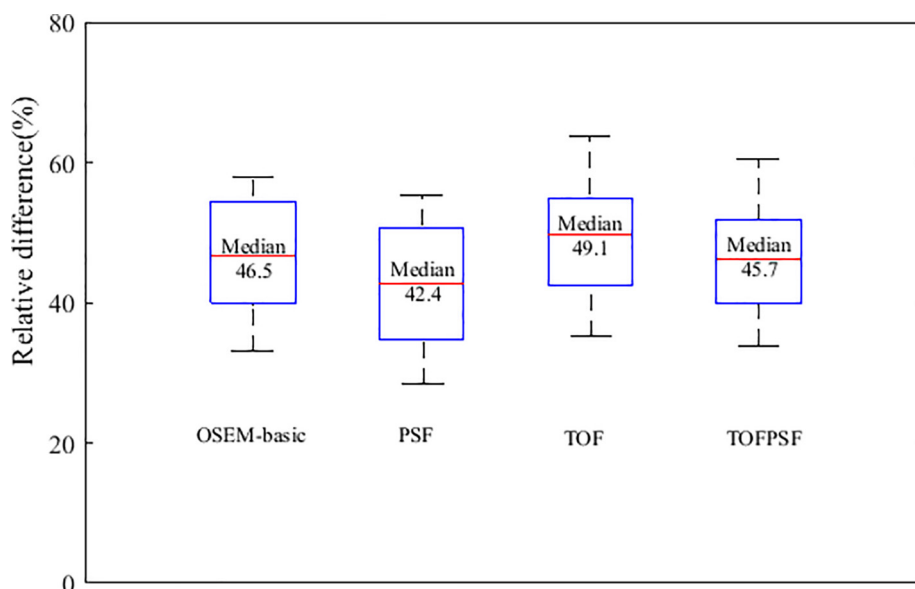


Fig. 5. Patient data. Box plots of relative differences (%) of the CNR in compensated images compared with the uncompensated images in patients with 42 lesions ≤ 30 in diameter for various reconstruction algorithms.

images. Overall, we found that quantitative parameters were affected by the choice of the reconstruction algorithms, lesion size and SBRs, and these effects increased with decreasing lesion sizes and SBRs. For example, the small spheres had a large relative difference in CR and CNR with various reconstruction algorithms. These findings suggest that reconstruction algorithms need to be chosen carefully when applying compensation methods.

There are some limitations to our study. Although we used different SBRs in phantom studies, we only considered fixed background activity. The number of retrospective patients was the other limitation in the present study. Furthermore, we analyzed all lesions without classification of the lesions into size groups, signal to background ratio and BMI, especially for heavy and obese patients. Another limitation is that with patient data, we did not know the ground truth CNR and other metric values. In this context, no-gold-standard techniques have been developed that can be used to assess the performance of different imaging methods on quantification tasks without ground truth [47–50]. The development and use of such techniques for assessing compensation methods with patient data is another area of future research.

5. Conclusion

We proposed and rigorously evaluated an image-based deconvolution method that incorporated wavelet-based denoising for combined compensation of respiratory motion and partial volume effects (PVEs) in oncologic PET images. The study demonstrates that the proposed method, and in particular, incorporation of a denoising method, can improve PET quantification performance. Our results provide evidence that quantitation is dependent on the choice of the reconstruction algorithm, especially when the signal support is small. The use of the proposed method can provide improved images reconstructed using OSEM-basic and TOF while only the respiratory compensation should be considered when applying TOFPSF. Overall, the choice of the combination of reconstruction algorithm and compensation method need to be determined carefully.

Acknowledgements

This work was supported under grant number 33381, Tehran University of Medical Sciences, as well as Masih Daneshvari Hospital and Shahid Beheshti University of Medical Sciences, Tehran, Iran. Abhinav K. Jha's efforts were supported by start-up funds from Washington University.

Conflict of interest

The authors declare that they have no conflict of interest.

References

- [1] El Naqa I. The role of quantitative PET in predicting cancer treatment outcomes. *Clin Transl Imaging* 2014;2:305–20.
- [2] O JH, Jacene H, Luber B, Wang H, Huynh MH, Leal JP, et al. Quantitation of cancer treatment response by 18F-FDG PET/CT: multicenter assessment of measurement variability. *J Nucl Med* 2017;58:1429–34.
- [3] Hughes NM, Mou T, Regan KNO, Murphy P, Sullivan JNO, Wolsztynski E, et al. Tumor heterogeneity measurement using [18F] FDG PET/CT shows prognostic value in patients with non-small cell lung cancer. *Eur. J. Hybrid Imaging* 2018;2:25.
- [4] Erlandsson K, Buvat I, Pretorius PH, Thomas BA, Hutton BF. A review of partial volume correction techniques for emission tomography and their applications in neurology, cardiology and oncology. *Phys Med Biol* 2012;57:R119–59.
- [5] Polycarpou I, Tsoumpas C, King AP, Marsden PK. Impact of respiratory motion correction and spatial resolution on lesion detection in PET: a simulation study based on real MR dynamic data. *Phys Med Biol* 2014;59:697–713.
- [6] Bal H, Guerin L, Casey ME, Conti M, Eriksson L, Michel C, et al. Improving PET spatial resolution and detectability for prostate cancer imaging. *Phys Med Biol* 2014;59:4411–26.
- [7] Dawood M, Buther F, Jiang Xiaoyi, Schafers KP. Respiratory motion correction in 3-D PET data with advanced optical flow algorithms. *IEEE Trans Med Imaging* 2008;27:1164–75.
- [8] Blume M, Martinez-Möller A, Keil A, Navab N, Rafecas M. Joint reconstruction of image and motion in gated positron emission tomography. *IEEE Trans Med Imaging* 2010;29:1892–906.
- [9] Dinges J, Nekolla SG, Bundschuh RA. Motion artifacts in oncological and cardiac PET imaging. *PET Clin* 2013;8:1–9.
- [10] Buther F, Vehren T, Schäfers KP, Schäfers M. Impact of data-driven respiratory gating in clinical PET. *Radiology* 2016;281:229–38.
- [11] Guerra L, De Ponti E, Morzenti S, Spadavecchia C, Crivellaro C. Respiratory motion management in PET/CT: applications and clinical usefulness. *Curr Radiopharm* 2017;10:85–92.
- [12] De Ponti E, Morzenti S, Crivellaro C, Elisei F, Crespi A, Guerra L. Motion management in PET/CT: technological solutions. *Curr Radiopharm* 2018;11:79–85.
- [13] Soret M, Bacharach SL, Buvat I. Partial-volume effect in PET tumor imaging. *J Nucl Med* 2007;48:932–45.
- [14] Rahmim A, Qi J, Sossi V. Resolution modeling in PET imaging: theory, Fpractice, benefits, and pitfalls. *Med Phys* 2013;40:064301.
- [15] Cysouw MCF, Kramer GM, Hoekstra OS, Frings V, de Langen AJ, Smit EF, et al. Accuracy and precision of partial volume correction in oncological PET/CT studies. *J Nucl Med* 2016;57:1642–9.
- [16] Hoetjes NJ, van Velden FHP, Hoekstra OS, Hoekstra CJ, Krak NC, Lammertsma AA, et al. Partial volume correction strategies for quantitative FDG PET in oncology. *Eur J Nucl Med Mol Imaging* 2010;37:1679–87.
- [17] Bettinardi V, Castiglioni I, De Bernardi E, Gilardi MC. PET quantification: strategies for partial volume correction. *Clin Transl Imaging* 2014;2:199–218.
- [18] Salavati A, Borofsky S, Boon-Keng TK, Houshmand S, Khiewwan B, Saboury B, et al. Application of partial volume effect correction and 4D PET in the quantification of FDG avid lung lesions. *Mol Imaging Biol* 2015;17:140–8.
- [19] Bousson N, Cheze Le Rest C, Hatt M, Visvikis D. Incorporation of wavelet-based denoising in iterative deconvolution for partial volume correction in whole-body PET imaging. *Eur J Nucl Med Mol Imaging* 2009;36:1064–75.
- [20] Wiemker R, Paulus T, Kabus S, Bülow T, Apostolova I, Buchert R, et al. Combined motion blur and partial volume correction for computer aided diagnosis of pulmonary nodules in PET/CT. *Int J Comput Assist Radiol Surg* 2008;3:105–13.
- [21] Chang G, Chang T, Pan T, Clark Jr JW, Mawlawi OR. Joint correction of respiratory motion artifact and partial volume effect in lung/thoracic PET/CT imaging. *Med Phys* 2010;37:6221–32.
- [22] Kadoya N, Fujita Y, Ito K, Dobashi S, Takeda K, Kishi K, et al. Investigation of correction method of recovery effect and motion blur for SUV quantification in FDG PET/CT in patients with early lung cancer. *J Nucl Med Radiat Ther* 2013;4:162–8.
- [23] Apostolova I, Wiemker R, Paulus T, Kabus S, Dreilich T, van den Hoff J, et al. Combined correction of recovery effect and motion blur for SUV quantification of solitary pulmonary nodules in FDG PET/CT. *Eur Radiol.* 2010;20:1868–77.
- [24] Andersen FL, Klausen TL, Loft A, Beyer T, Holm S. Clinical evaluation of PET image reconstruction using a spatial resolution model. *Eur J Radiol* 2013;82:862–9.
- [25] Vennart NJ, Bird N, Buscombe J, Cheow HK, Nowosinska E, Heard S. Optimization of PET/CT image quality using the GE “Sharp IR” point-spread function reconstruction algorithm. *Nucl Med Commun* 2017;38:471–9.
- [26] Conti M, Bendriem B. The new opportunities for high time resolution clinical TOF PET. *Clin Transl Imaging* 2019;7:139–47.
- [27] Merlin T, Visvikis D, Fernandez P, Lamare F. A novel partial volume effects correction technique integrating deconvolution associated with denoising within an iterative PET image reconstruction. *Med Phys* 2015;42:804–19.
- [28] Taniguchi T, Akamatsu G, Kasahara Y, Mitsumoto K, Baba S, Tsutsui Y, et al. Improvement in PET/CT image quality in overweight patients with PSF and TOF. *Ann Nucl Med* 2015;29:71–7.
- [29] Schaeferkoetter JD, Yan J, Sjolholm T, Townsend DW, Conti M, Tam JKC, et al. Quantitative accuracy and lesion detectability of low-dose 18F-FDG PET for lung cancer screening. *J Nucl Med* 2017;58:399–405.
- [30] Ketabi A, Ghafarian P, Mosleh-Shirazi MA, Mahdavi SR, Rahmim A, Ay MR. Impact of image reconstruction methods on quantitative accuracy and variability of FDG-PET volumetric and textural measures in solid tumors. *Eur Radiol* 2019;29:2146–56.
- [31] Rogasch JM, Steffen IG, Hofheinz F, Großer OS, Furth C, Mohnike K, et al. The association of tumor-to-background ratios and SUVmax deviations related to point spread function and time-of-flight F18-FDG-PET/CT reconstruction in colorectal liver metastases. *EJNMMI Res.* 2015;5:31.
- [32] Boellaard R, Delgado-Bolton R, Oyen WJG, Giammarile F, Tatsch K, Eschner W, et al. EANM procedure guidelines for tumour imaging: version 2.0. *Eur J Nucl Med Mol Imaging* 2015;42:328–54.
- [33] Xu Q, Yuan K, Ye D. Respiratory motion blur identification and reduction in ungated thoracic PET imaging. *Phys Med Biol* 2011;56:4481–98.
- [34] Zhou D, Shen X. Image denoising using block thresholding. *Congress on Image and Signal Processing.* Washington, DC: IEEE; 2008. p. 335–8.
- [35] Chang SG, Yu B, Vetterli M. Adaptive wavelet thresholding for image denoising and compression. *IEEE Trans Image Process* 2000;9:1532–46.
- [36] Siman W, Mawlawi OR, Mikkell JK, Mourada F, Kappadath SC. Effects of image noise, respiratory motion, and motion compensation on 3D activity quantification in count-limited PET image. *Phys Med Biol* 2017;62:448–64.
- [37] Daube-Witherspoon ME, Surti S, Perkins AE, Karp JS. Determination of accuracy and precision of lesion uptake measurements in human subjects with time-of-flight PET. *J Nucl Med* 2014;55:602–7.
- [38] Suljic A, Tomse P, Jensterle L, Skrk D. The impact of reconstruction algorithms and time of flight information on PET/CT image quality. *Radiol Oncol* 2015;49:227–33.
- [39] Akamatsu G, Mitsumoto K, Taniguchi T, Tsutsui Y, Baba S, Sasaki M. Influences of point-spread function and time-of-flight reconstructions on standardized uptake value of lymph node metastases in FDG-PET. *Eur J Radiol* 2014;83:226–30.

- [40] Nehmeh SA. Respiratory motion correction strategies in thoracic PET-CT imaging. *PET Clin* 2013;8:29–36.
- [41] Fayad H, Schmidt H, Kuestner T, Visvikis D. 4D MR and attenuation map generation in PET/MR imaging using 4D PET derived deformation matrices: a feasibility study for lung cancer applications. *J Nucl Med* 2016;33:1–25.
- [42] Mehranian A, Zaidi H. Impact of time-of-flight PET on quantification errors in MR imaging-based attenuation correction. *J Nucl Med* 2015;56:635–41.
- [43] Sharifpour R, Ghafarian P, Bakhshayesh-Karam M, Jamaati H, Ay MR. Impact of time-of-flight and point-spread-function for respiratory artifact reduction in PET/CT imaging: focus on SUV. *Tanaffos* 2017;16:127–35.
- [44] Schaefferkoetter J, Casey M, Townsend D, Fakhri GE. Clinical impact of time-of-flight and point response modeling in PET reconstructions: a lesion detection study. *Phys Med Biol* 2013;58:1465–78.
- [45] Shekari M, Ghafarian P, Ahangari S, Ay MR. Quantification of the impact of TOF and PSF on PET images using the noise-matching concept: clinical and phantom study. *Nucl Sci Technol* 2017;28:167.
- [46] Sharifpour R, Ghafarian P, Rahmim A, Ay MR. Quantification and reduction of respiratory induced artifacts in positron emission tomography/computed tomography using the time-of-flight technique. *Nucl Med Commun* 2017;38:948–55.
- [47] Kupinski MA, Hoppin JW, Krasnow J, Dahlberg S, Leppo JA, King MA, et al. Comparing cardiac ejection fraction estimation algorithms without a gold standard. *Acad Radiol* 2006;13:329–37.
- [48] Jha AK, Kupinski MA, Rodríguez JJ, Stephen RM, Stopeck AT. Task-based evaluation of segmentation algorithms for diffusion-weighted MRI without using a gold standard. *Phys Med Biol* 2012;57:4425–46.
- [49] Jha AK, Caffo B, Frey EC. A no-gold-standard technique for objective assessment of quantitative nuclear-medicine imaging methods. *Phys Med Biol* 2016;61:2780–800.
- [50] Jha AK, Mena E, Caffo B, Ashrafinia S, Rahmim A, Frey E, et al. Practical no-gold-standard evaluation framework for quantitative imaging methods: application to lesion segmentation in positron emission tomography. *J Med Imaging (Bellingham)* 2017;4:011011.